Enhanced Strength Through Nanotwinning in the Thermoelectric Semiconductor InSb

Guodong Li,[1,2,‡] Sergey I. Morozov,[3] Qingjie Zhang,[1,*] Qi An,[4,†] Pengcheng Zhai,[1] and G. Jeffrey Snyder[2]

[1]*State Key Laboratory of Advanced Technology for Materials Synthesis and Processing,*
Wuhan University of Technology, Wuhan 430070, China
[2]*Department of Materials Science and Engineering, Northwestern University, Evanston, Illinois 60208, USA*
[3]*Department of Computer Simulation and Nanotechnology, South Ural State University, Chelyabinsk 454080, Russia*
[4]*Department of Chemical and Materials Engineering, University of Nevada, Reno, Reno, Nevada 89557, USA*

The conversion efficiency (zT) of thermoelectric (TE) materials has been enhanced over the last two decades, but their engineering applications are hindered by the poor mechanical properties, especially the low strength at working conditions. Here we used density functional theory (DFT) to show a strength enhancement in the TE semiconductor InSb arising from the twin boundaries (TBs). This strengthening effect leads to an 11% enhancement of the ideal shear strength in flawless crystalline InSb where this theoretical strength is considered as an upper bound on the attainable strength for a realistic material. DFT calculations reveal that the directional covalent bond rearrangements at the TB accommodating the structural mismatch lead to the anisotropic resistance against the deformation combined with the enhanced TB rigidity. This produces a strong stress response in the nanotwinned InSb. This work provides a fundamental insight for understanding the deformation mechanism of nanotwinned TE semiconductors, which is beneficial for developing reliable TE devices.

The overconsumption of fossil fuels is causing a severe environmental impact of global climate change. Thus, it is becoming increasingly urgent for seeking alternative clean and sustainable energy sources. Thermoelectric (TE) conversion technology could play a significant role in a global sustainable energy solution because it has the capability of directly converting heat into electricity with no CO_2 production, no moving parts, silence, and scalability [1]. Good TE materials should possess simultaneously excellent mechanical properties and high conversion efficiency (zT). The zT value of TE materials has improved remarkably during the last two decades [2–6], but the mechanical properties of TE materials remain the bottleneck of their commercial applications. In engineering applications of TE devices, the unavoidable thermomechanical stresses from cycling of the temperature gradients easily cause rapid deterioration of material performance and accelerated failure of TE devices [7,8]. Therefore, robust TE materials require excellent mechanical properties such as high mechanical strength and toughness.

It is well established that grain boundaries (GBs) play a significant role in strengthening or weakening polycrystalline materials. GB strengthening can be achieved through the grain size reduction by pinning mobile dislocations, well known as the Hall-Petch effect [9,10]. However, below a threshold grain size, GB sliding or migration dominates the plastic deformation, weakening materials by further reducing the grain size [11,12]. Twin boundaries (TBs), more energetically stable than normal GBs, show a much stronger strengthening compared with normal GBs [13–15]. For

example, nanotwinned Cu shows a tensile superstrength about ten times higher than that of conventional coarse-grained polycrystalline Cu [16]. An unusual TB in boron nitride produces a large strength enhancement under indentation compression [17]. These trends are widely investigated in crystalline metals and ceramics [13–17], but they are seldom studied in TE semiconductors.

Engineering GBs has been recently found to be an effective strategy to reduce the thermal conductivity and enhance the zT value of TE materials [18–21]. For example, dense dislocation arrays formed at low-energy GBs in $Bi_{0.5}Sb_{1.5}Te_3$ substantially lower the lattice thermal conductivity, leading to a dramatically improved zT value of 1.86 at 320 K [18]. A similar strategy has been applied to other high-performance TE materials such as $CoSb_3$ [19], Mg_2Si [20], and PbTe [21]. In addition, it was observed that the phonon scatting induced by TBs can further decrease the lattice thermal conductivity [22]. Despite the important roles of TBs in material properties, their effects on the mechanical properties remain unknown.

Here, we apply density functional theory (DFT) at the level of the Perdew-Burke-Ernzerhof (PBE) functional to investigate the mechanical strength, deformation, and failure mechanism of flawless and nanotwinned TE InSb under both pure shear and biaxial shear deformations, respectively. We find that the mechanical strength of the nanotwinned structure is 11% higher than that of the flawless crystal, which is against the general understanding that structural defects lower the mechanical strength. This strengthening effect originates from the enhanced structural rigidity due to

the directional covalent bond rearrangements at the TBs. This novel TB dominated strengthening effect can be widely used to design and develop robust TE devices.

All simulations were performed with the Vienna *ab initio* simulation package (VASP), using the PBE functional and the projector augmented wave (PAW) method to account for the core-valence interactions [23–26]. The convergence for terminating the electronic self-consistent field and the force criterion were set to less than 1×10^{-6} eV and 1×10^{-2} eV/Å, respectively. An energy cutoff of 500 eV with a Monkhorst-Pack grid of $7 \times 7 \times 7$ in the k-space was adopted for the geometry optimization. The electron localization function (ELF) of the optimized structure was calculated to analyze the chemical bonding conditions [27]. The elastic constants (C_{ij}) were computed from the stress-strain relationship as a function of various cell distortions $\delta(\delta < 3\%)$ from the optimized structure. Then, the isotropic polycrystalline elastic moduli can be derived using the Voigt-Reuss-Hill method [28].

To perform the pure shear deformation, we imposed the shear strain on a specific slip system while allowing full relaxation along the other five strain components. To simulate the stress conditions under indentation experiment, we applied biaxial shear deformation by constraining the ratio of shear stress to normal stress and relating it to the geometry of indenter, while the structure is relaxed along another four strain components. The simulation details could be found in our previous study [29].

InSb thermoelectric compound crystallizes in the cubic ZnS structure which belongs to the space group $F\bar{4}3m$ (space group number 216) where the In and Sb atom occupy the $4a$ (0,0,0) and $4c$ (0.25,0.25,0.25) sites, respectively, as shown in Fig. S1 of Supplemental Material (SM) [30]. The unit cell contains 4 In and 4 Sb atoms, and each Sb atom is tetrahedrally coordinated with 4 In atoms forming the $SbIn_4$ framework. The shared electron pair between In and Sb atoms suggests that the In—Sb forms a covalent bond with a bond distance of 2.88 Å [30]. Our PBE gives an equilibrium lattice parameter of $a = 6.648$ Å, which agrees very well with the previous theoretical prediction of $a = 6.633$ Å [31], and is only 2.6% larger than the experimental value of $a = 6.476$ Å at 300 K [32].

To examine the structure-property relationship, we computed the elastic properties to provide basic understanding about the rigidity and stability of InSb. The predicted elastic constants for InSb are $C_{11} = 54.26$ GPa, $C_{22} = 28.56$ GPa, and $C_{44} = 24.73$ GPa. This leads to a calculated Young's modulus $E = 48.72$ GPa, bulk modulus $B = 37.12$ GPa, shear modulus $G = 19.02$ GPa, and Poisson's ratio $v = 0.28$ using the Voigt-Reuss-Hill method [28]. Our predicted elastic moduli of InSb show a good agreement with the previous *ab initio* calculation using the PBE functional [31], but are much lower than those of other covalent TE compounds such as TiNiSn ($E=171.65$ GPa, $B= 128.78$ GPa, $G=67.16$ GPa) and $CoSb_3$ ($E = 145.38$ GPa,

$B = 87.38$ GPa, $G = 59.45$ GPa) [33,34]. This suggests that InSb has a much weaker structural stiffness compared with TiNiSn and $CoSb_3$. The Poisson's ratio v, which is a significant elastic property that relates to a material's lateral deformation, can be used to estimate a material's brittleness or ductility [35,36]. Our predicted v is 0.28 for InSb, suggesting that it is brittle according to Frantsevich's criterion [35,36] in which the v value for brittle materials is less than 0.33.

To understand the mechanical properties under deformation, we examined the shear-stress-shear-strain relations of InSb along various slip systems of $(001)\langle 100 \rangle$, $(001)\langle 110 \rangle$, $(111)\langle 11\bar{2} \rangle$, and $(111)\langle \bar{1}\,\bar{1}\,2 \rangle$ [Fig. 1(a)]. Among all the shear paths, the $(111)\langle 11\bar{2} \rangle$ slip system has the lowest ideal strength of 2.43 GPa at the critical shear strain of 0.311, suggesting this is the most plausible slip system. This value is much lower than those of TiNiSn (10.52 GPa) and $CoSb_3$ (7.17 GPa) [33,34], which is consistent with the above calculations on the elastic modulus. For the $(111)\langle \bar{1}\,\bar{1}\,2 \rangle$ slip system that corresponds to the opposite shear direction of $(111)\langle 11\bar{2} \rangle$, the ideal shear stress is 3.82 GPa, which is
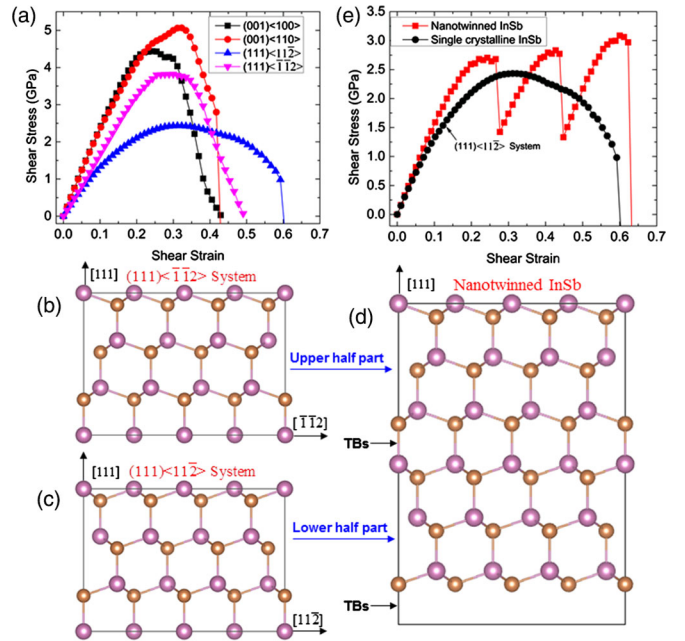

FIG. 1. The shear-stress-shear-strain relationships and atomic structures for crystal and nanotwinned InSb. (a) Stress-strain relations for crystal InSb along various slip systems; (b) atomic structure for crystalline InSb along the $(111)\langle \bar{1}\,\bar{1}\,2 \rangle$ slip system. This cell contains $24 \times$ In and $24 \times$ Sb atoms, (c) atomic structure for crystalline InSb along the $(111)\langle 11\bar{2} \rangle$ slip system; and (d) nanotwinned InSb structure with the TB along the {111} plane. This cell contains $48 \times$ In and $48 \times$ Sb atoms. The upper half consists of the $(111)\langle \bar{1}\,\bar{1}\,2 \rangle$ system of InSb [Fig. 1(b)], and the lower half part consists of the $(111)\langle 11\bar{2} \rangle$ system of InSb [Fig. 1(c)]. The twin spacing is 1.0 nm; (e) stress-strain relations for nanotwinned InSb, as well as the comparison with crystalline InSb along the most plausible slip system $(111)\langle 11\bar{2} \rangle$.

57.2% larger than the $(111)\langle11\bar{2}\rangle$ slip system, but it is significantly lower than those (4.44 and 5.07 GPa) along the $(001)\langle100\rangle$ and $(001)\langle110\rangle$ directions. This suggests that the most plausible slip plane for InSb is the $\{111\}$ plane, which is similarly found in other isotypic covalent solids such as BN and diamond [37]. As such, we constructed the nanotwinned structure with the TBs along the $\{111\}$ plane as shown in Fig. 1(d), which have been observed in experiments [22]. This TB leads to a predicted twin interfacial energy of 20.7 mJ/m^2. Such lower interfacial energy for InSb might arise from the easy structural modification due to the directional bond rearrangements along the TBs [Fig. 1(d)] [37]. This also explains why these twin defects are easy to form experimentally [22].

To investigate the effect of nanotwins on mechanical strength, we probed the stress-strain relations of crystal and nanotwinned InSb [Fig. 1(e)]. The shear strength (the first maximum shear stress) of nanotwinned InSb is 2.70 GPa at shear strain of 0.266. This value is 11% larger than that (2.43 GPa) of the flawless crystal. The ideal strength of a flawless crystal is usually considered as an upper bound for a realistic material because the presence of defects such as dislocations, GBs, and cracks is considered to weaken a material [15]. However, we show from DFT that the ideal shear strength of flawless InSb could be enhanced by 11% through a TB strategy, even though the nanotwinned structure is less stable than the flawless crystal thermodynamically.

To understand the strengthening effect from nanotwins in InSb, we examined the structural evolution and bond-responding processes in flawless and nanotwinned InSb, respectively. Figure 2 displays the structural patterns and typical bond changes of crystalline InSb at critical shear strains shearing along the $(111)\langle11\bar{2}\rangle$ and $(111)\langle\bar{1}\,\bar{1}\,2\rangle$ slip systems. For the most plausible slip system of $(111)\langle11\bar{2}\rangle$, the structure continuously resists the deformation without breaking bond until the shear strain of 0.592 [Fig. 2(a)]. With further increasing shear strain, the In1—Sb1 covalent bond breaks, collapsing the structure and relaxing the shear stress, hence leading to the structural failure [Fig. 2(b)]. To understand the failure mechanism, Fig. 2(c) plots the typical bond lengths (In1—Sb1 and In2—Sb1) and the bond angle (In3—Sb1—In2 and In3—Sb1—In1) as the shear strain increases to failure. As shear strain increases to 0.311 corresponding to the maximum shear stress, the In2—Sb1 bond is stretched while the In1—Sb1 bond shrinks, resisting the deformation. With further increasing shear strain to 0.592, the In1—Sb1 bond starts to stretch while the In2—Sb1 bond deforms with a much smaller stretching ratio. These structural changes suggest that the structural stiffness gradually softens at this stage, leading to the decreasing shear stress [Fig. 1(a)]. Before the structural failure, the In3—Sb1—In2 angle linearly increases while the In3—Sb1—In1 angle linearly decreases accommodating the shear deformation. At the fracture strain of 0.605, the
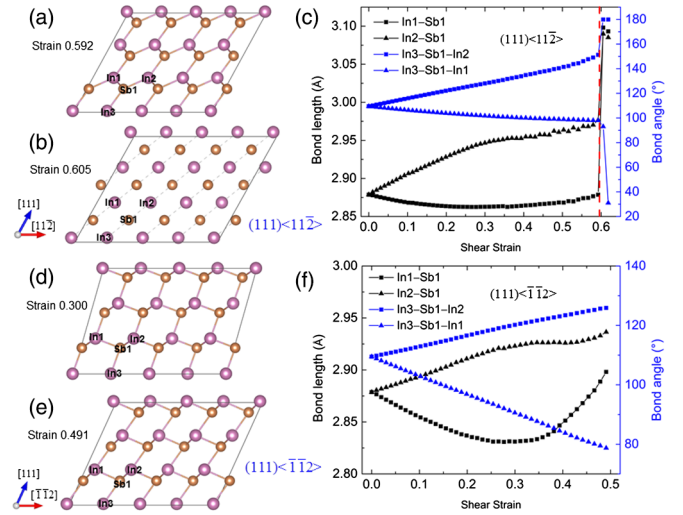

FIG. 2. The structural deformation and bond-responding processes for crystalline InSb shear along the $(111)\langle11\bar{2}\rangle$ and $(111)\langle\bar{1}\,\bar{1}\,2\rangle$ slip systems. (a) Structure at 0.592 shear strain before failure in the $(111)\langle11\bar{2}\rangle$ system. (b) Structure at failure strain of 0.605 in the $(111)\langle11\bar{2}\rangle$ system. The dashed lines between In2 and Sb1 atoms represent their weak or nonbonding interactions. (c) The typical bond lengths (In1—Sb1 and In2—Sb1) and the bond angles (In3—Sb1—In2 and In3—Sb1—In1) with the increasing shear strain in the $(111)\langle11\bar{2}\rangle$ system. The red dashed line in Fig. 2(c) represents the strain just before failure. (d) Structure at 0.300 shear strain corresponding to the ideal shear strength in the $(111)\langle\bar{1}\,\bar{1}\,2\rangle$ system. (e) Structure at failure strain of 0.491 in the $(111)\langle\bar{1}\,\bar{1}\,2\rangle$ system. (f) The average bond lengths (In1—Sb1 and In2—Sb1) and the bond angles (In3—Sb1—In2 and In3—Sb1—In1) with the increasing shear strain in the $(111)\langle\bar{1}\,\bar{1}\,2\rangle$ system.

In1—Sb1 bond suddenly increases from 2.88 to 3.10 Å, representing the bond breaking. This relaxes the shear stress to 0, resulting in the failure of InSb.

The opposite slip system $((111)\langle\bar{1}\,\bar{1}\,2\rangle)$ shows the similar structural deformations, as shown in Figs. 2(d)–2(f). However, at the critical shear strain corresponding to the ideal strength, the In1—Sb1 bond shrinks to 2.83 Å, which shows a larger reduction compared with that (2.86 Å) in the slip system $(111)\langle11\bar{2}\rangle$. This suggests that the structural stiffness of the $(111)\langle\bar{1}\,\bar{1}\,2\rangle$ system is much stronger in resisting the deformation than that of the $(111)\langle11\bar{2}\rangle$, well explaining why the $(111)\langle\bar{1}\,\bar{1}\,2\rangle$ system shows a much higher maximum shear strength of 3.82 GPa compared with the $(111)\langle11\bar{2}\rangle$ system (2.43 GPa). In addition, unlike the $(111)\langle11\bar{2}\rangle$ system, the In1—Sb1 bond is rapidly stretched starting from the critical shear strain of 0.311 in the $(111)\langle\bar{1}\,\bar{1}\,2\rangle$ system, indicating that the structure stiffness dramatically decreases. This leads to a much sharper stress decrease beyond the maximum shear stress point in the $(111)\langle\bar{1}\,\bar{1}\,2\rangle$ system observed in Fig. 1(a). Moreover, we also find that the deformation mechanism of InSb along the $(001)\langle100\rangle$ and $(001)\langle110\rangle$ slip systems is similar with that
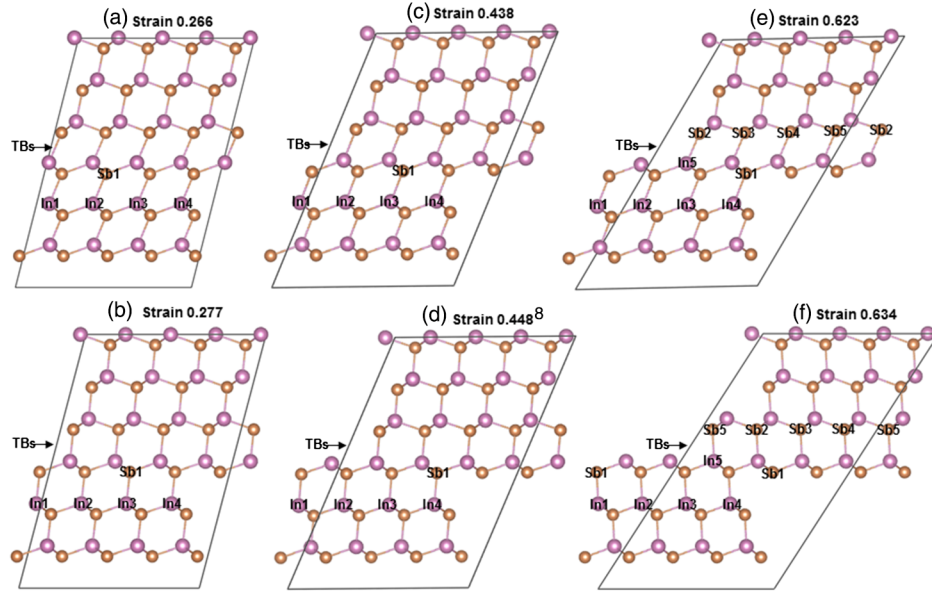
FIG. 3. Structural changes of nanotwinned InSb. (a) Structure at 0.266 shear strain, which corresponds to the ideal shear strength. (b) Structure at 0.277 shear strain. The In2—Sb1 covalent bond breaks and a new In3—Sb1 bond forms, which moves the lower half part left by one "In-Sb hexagon." (c) Structure at 0.438 shear strain before the structural rearrangement. (d) Structure at 0.448 shear strain. The In3—Sb1 covalent bond breaks and a new In4—Sb1 bond forms, which moves the lower half part left by one more "In-Sb hexagon". (e) Structure at 0.623 shear strain before the structural failure. (f) Structure at failure strain of 0.634. The In4—Sb1 covalent bond breaks and a new In1—Sb1 bond forms, which again moves the lower half left by one more "In-Sb hexagon." The In5—Sb2 bond in the TBs breaks while the In5—Sb5 bond forms, which totally releases the shear stress and results in the structural failure.

along the $(111)\langle 11\bar{2}\rangle$ direction, as displayed in Figs. S2 and S3 in the SM [30].

Figures 3 and S4 in the SM display the structural and bond changes of nanotwinned InSb to investigate the strengthening effect. With the shear strain increasing to 0.266 corresponding to the ideal strength point, we surprisingly find that the TBs coupling the upper $((111)\langle 11\bar{2}\rangle$ system) and lower $((111)\langle \bar{1}\,\bar{1}\,2\rangle)$ half parts could resist shear deformation without any bond softening or breakage [Fig. 3(a)]. As shown in Fig. S4, the In5—Sb2 bond in the TBs is stretched with a smaller stretching ratio compared with the In2—Sb1 bond in the lower half part, suggesting the stiffness of TBs is slightly stronger than that of the lower part. More importantly, the upper half is much stronger in resisting the deformation than the lower half as discussed above, suggesting that the nanotwinned structure has a much stronger assembled structure stiffness than the $(111)\langle 11\bar{2}\rangle$ slip system. This explains why the maximum shear strength of nanotwinned InSb can exceed the ideal shear strength of crystalline InSb along the $(111)\langle 11\bar{2}\rangle$ direction, as shown in Fig. 1(e).

For nanotwinned InSb, the failure exhibits a three-step process. (i) As the shear strain increases from 0.266 to 0.277, the stretched In2—Sb1 covalent bond sharply increases from 2.95 to 5.87 Å (Fig. S4), breaking this bond. Meanwhile, the In3—Sb1 distance reduces from 4.60 to 2.84 Å (Fig. S4), forming a new covalent bonding. This bond breaking-formation process moves the lower half part left by one

"In-Sb hexagon" [Fig. 3(b)]. This rearranged structure releases the shear stress from 2.77 to 1.33 GPa [Fig. 1(e)], while it could further resist the deformation with increasing shear strain. (ii) As the shear strain increases from 0.438 to 0.448, the same bond breaking-formation process (the In3—Sb1 bond breaks while the In4—Sb1 bond forms) occurs, which moves the lower part left by one more "In-Sb hexagon" [Figs. 3(c) and 3(d)]. (iii) With the shear strain increasing from 0.623 to 0.634, the In4—Sb1 bond breaks while the In1—Sb1 bond forms, which again moves the lower part left. However, in the TB region, the In5—Sb2 bond breaks while the In5—Sb5 bond forms [Figs. 3(e) and 3(f)]. This significant structural rearrangement in the TBs totally releases the shear stress [Fig. 1(e)], resulting in the failure of the nanotwinned structure.

To further understand the strengthening in nanotwinned InSb, we also used DFT to apply biaxial shear deformation to the nanotwinned structure mimicking the stress conditions under indentation experiments, and compared this with the flawless crystal.

Figure 4(a) displays the calculated shear-stress-shear-strain relationships for biaxial shear deformation. The flawless crystal experiences an obvious yielding deformation for shear strains ranging from 0.210 to 0.311, and then has a sudden stress drop representing the mechanical failure. This stress response is similar to our previously predicted results for pure shear deformation [Fig. 1(e)]. For the nanotwinned structure, however, the shear stress suddenly
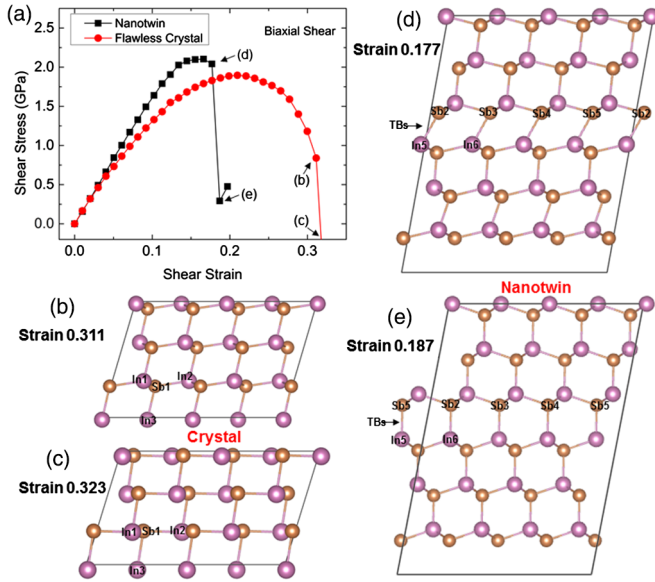
FIG. 4. Stress responses and structural patterns of nanotwinned and flawless crystal InSb under biaxial shear deformation. The flawless crystal is sheared along the $(111)\langle11\bar{2}\rangle$ slip system. (a) Shear-stress–shear-strain relations; (b) atomic structure at 0.311 strain for flawless crystal before the failure; (c) atomic structure at a failure strain of 0.323 for flawless crystal; (d) atomic structure at 0.177 strain for the nanotwinned InSb before the failure; and (e) the failure structure at 0.187 strain for the nanotwinned InSb.

drops beyond the maximum stress point. This one-step failure process is different from the three-step process observed in pure shear deformation [Fig. 1(e)]. The maximum shear stress for the nanotwinned structure is 2.10 GPa, which also exceeds the strength limit (1.90 GPa) for the flawless crystal by 10.52%. The biaxial shear simulation shows the same TB strengthening effect as for pure shear deformation. This suggested that the strengthening effects could be verified through indentation experiments if other defects (such as vacancies, GBs, etc.) can be ignored.

Figures 4(b)–4(e) and Figs. S5 and S6 display the structural patterns and bond responses to understand the underlying strengthening mechanism under biaxial shear deformation. For the flawless crystal, the failure deformation [Figs. 4(b) and 4(c)] under indentation is significantly different from that [Figs. 2(a) and 2(b)] under pure shear deformation. The "In-Sb hexagon" gradually approaches an "In-Sb tetragon" until the mechanical failure. Under biaxial shear deformation, the In2—Sb1 bond first shrinks and then is stretched starting at 0.123 strain, while the In1—Sb1 bond is first stretched slightly and then shrinks before the failure (Fig. S5). At failure strain of 0.323, the In2—Sb1 length suddenly increases to 3.04 Å, suggesting the bond breakage. This releases the shear stress and collapses the structure. Compared with the bond responses for pure shear deformation [Fig. 2(c)], we find that the compression suppresses the stretching of the In1—Sb1 bond and the bending of the

In3—Sb1—In2 bond angle because of the normal stress. This indicates that the compression plays a significant role in modifying the deformation mechanism, which is similarly found in the $(111)\langle\bar{1}\,\bar{1}\,2\rangle$ slip system as shown in Fig. S7. For the nanotwinned structure, the TB is distorted more severely compared with the upper and lower parts in resisting the deformation [Fig. 4(d)]. At failure strain of 0.187, the In5—Sb2 bond breaks while the In5—Sb2 bond forms, which releases the stress and rearranges the TB [Fig. 4(e)]. The bond changes (Fig. S6) in the TB clearly illustrate this bond breaking-formation process. Compared with the pure shear deformation, the concomitant compression modifies the deformation mechanism of nanotwinned structure because the In—Sb bond in the lower half part is suppressed from breakage. However, due to the much stronger structural rigidity in the nanotwinned InSb, the same TB-dominated strengthening effect is observed in the indentation stress conditions.

A similar strengthening effect, which arises from new bonding formation in the TBs, was observed in TE semiconductor Bi_2Te_3 [38]. Recent experimental results reported that nanotwinned Bi_2Te_3 exhibits an eightfold and a sixfold increase in the compressive and flexural strength, respectively, validating the theoretical prediction [39]. The TB strengthening, originating from either the directional covalent bond rearrangements in nanotwinned InSb or the bonding formation in nanotwinned Bi_2Te_3, is an effective strategy in improving the strength of TE materials.

In summary, we used DFT to investigate the role of TBs on mechanical properties of covalent TE semiconductor InSb, demonstrating that the intrinsic mechanical strength of InSb can be exceeded by 11% through a TB-dominated planar defect. This strengthening stems from anisotropic shear-stress response in the upper and lower halves of the nanotwinned structure, as well as enhanced structural rigidity due to the directional covalent bond rearrangements at the TB. This strengthening mechanism should be applicable to other low strength semiconductors, e.g., GaAs and ZnSe, that possess a similar crystalline structure and possibly other weak materials that can support such nanotwins.

*Corresponding author.
zhangqj@whut.edu.cn
†Corresponding author.
qia@unr.edu
‡Corresponding author.
guodonglee@whut.edu.cn

[1] G. J. Snyder and E. S. Toberer, Nat. Mater. **7**, 105 (2008).
[2] T. Zhu, Y. Liu, C. Fu, J. P. Heremans, J. G. Snyder, and X. Zhao, Adv. Mater. **29**, 1605884 (2017).
[3] Y. Zhou and L. D. Zhao, Adv. Mater. 1702676 (2017).
[4] Y. Z. Pei, X. Y. Shi, A. LaLonde, H. Wang, L. D. Chen, and G. J. Snyder, Nature (London) **473**, 66 (2011).
[5] Y. L. Tang, Z. M. Gibbs, L. A. Agapito, G. Li, H. S. Kim, M. B. Nardelli, S. Curtarolo, and G. J. Snyder, Nat. Mater. **14**, 1223 (2015).
[6] L. D. Zhao, S. H. Lo, Y. Zhang, H. Sun, G. Tan, C. Uher, C. Wolverton, V. P. David, and M. G. Kanatzidis, Nature (London) **508**, 373 (2014).
[7] D. G. Zhao, H. R. Geng, and L. D. Chen, Int. J. Appl. Ceram. Technol. **9**, 733 (2012).
[8] K. H. Bae, S. M. Choi, K. H. Kim, H. S. Choi, W. S. Seo, I. H. Kim, S. Lee, and H. J. Hwang, J. Electron. Mater. **44**, 2124 (2015).
[9] E. O. Hall, Proc. Phys. Soc. London Sect. B **64**, 747 (1951).
[10] N. J. Petch, J. Iron Steel Inst. **174**, 25 (1953).
[11] T. J. Rupert, D. S. Gianola, Y. Gan, and K. J. Hemker, Science **326**, 1686 (2009).
[12] J. Schiotz and K. W. Jacobsen, Science **301**, 1357 (2003).
[13] K. Lu, L. Lu, and S. Suresh, Science **324**, 349 (2009).
[14] K. M. Reddy, J. J. Guo, Y. Shinoda, T. Fujita, A. Hirata, J. P. Singh, J. W. McCauley, and M. W. Chen, Nat. Commun. **3**, 1052 (2012).
[15] Q. An, W. A. Goddard, K. Y. Xie, G. D. Sim, K. J. Hemker, T. Munhollon, M. F. Toksoy, and R. A. Haber, Nano Lett. **16**, 7573 (2016).
[16] L. Lu, X. Chen, X. Huang, and K. Lu, Science **323**, 607 (2009).
[17] Y. J. Tian, B. Xu, D. L. Yu, Y. M. Ma, Y. B. Wang, Y. B. Jiang, W. T. Hu, C. C. Tang, Y. F. Gao, K. Luo, Z. S. Zhao, L. M. Wang, B. Wen, J. L. He, and Z. Y. Liu, Nature (London) **493**, 385 (2013).
[18] S. Il Kim, K. H. Lee, H. A. Mun, H. S. Kim, S. W. Hwang, J. W. Roh, D. J. Yang, W. H. Shin, X. S. Li, Y. H. Lee, G. J. Snyder, and S. W. Kim, Science **348**, 109 (2015).
[19] X. Meng, Z. Liu, B. Cui, D. Qin, H. Geng, W. Cai, L. Fu, J. He, Z. Ren, and J. Sui, Adv. Energy Mater. 1602582 (2017).
[20] J. Z. Xin, H. J. Wu, X. H. Liu, T. J. Zhu, G. T. Yu, and X. B. Zhao, Nano Energy **34**, 428 (2017).
[21] Z. W. Chen, B. H. Ge, W. Li, S. Q. Lin, J. W. Shen, Y. J. Chang, R. Hanus, G. J. Snyder, and Y. Z. Pei, Nat. Commun. **8**, 13828 (2017).
[22] J. Mao, Y. Wang, Z. Liu, B. Ge, and Z. Ren, Nano Energy **32**, 174 (2017).
[23] G. Kresse and J. Furthmuller, Comput. Mater. Sci. **6**, 15 (1996).
[24] G. Kresse and J. Furthmuller, Phys. Rev. B **54**, 11169 (1996).
[25] G. Kresse and D. Joubert, Phys. Rev. B **59**, 1758 (1999).
[26] J. P. Perdew, K. Burke, and M. Ernzerhof, Phys. Rev. Lett. **77**, 3865 (1996).
[27] B. Silvi and A. Savin, Nature (London) **371**, 683 (1994).
[28] D. H. Chung, Philos. Mag. **8**, 833 (1963).
[29] G. Li, U. Aydemir, M. Wood, Q. An, W. A. Goddard, P. Zhai, Q. Zhang, and G. J. Snyder, J. Mater. Chem. A **5**, 9050 (2017).
[30] See Supplemental Material at http://link.aps.org/supplemental/10.1103/PhysRevLett.119.215503 for a detailed description of the crystal structure of the thermoelectric InSb compound; the bond-responding process of single crystalline InSb along the $(001)\langle100\rangle$ and $(001)\langle110\rangle$ slip system, respectively; typical bond changes of nanotwinned InSb under pure shear deformation; the bond-responding processes for the $(111)\langle11\bar{2}\rangle$ flawless crystal and nanotwinned InSb under biaxial shear deformation; biaxial shear deformation of crystal InSb for shearing along the $(111)\langle\bar{1}\,\bar{1}\,2\rangle$ slip system, and a comparison with the pure shear deformation.
[31] M. de Jong, W. Chen, T. Angsten, A. Jain, R. Notestine, A. Gamst, M. Sluiter, C. K. Ande, S. van der Zwaag, J. J. Plata, C. Toher, S. Curtarolo, G. Ceder, K. A. Persson, and M. Asta, Sci. Data. **2**, 150009 (2015).
[32] K. Ersching, C. E. M. Campos, J. C. Lima de, and T. A. Grandi, Mater. Chem. Phys. **112**, 745 (2008).
[33] G. D. Li, Q. An, U. Aydemir, W. A. Goddard, M. Wood, P. C. Zhai, Q. J. Zhang, and G. J. Snyder, J. Mater. Chem. A **4**, 14625 (2016).
[34] G. D. Li, Q. An, W. J. Li, W. A. Goddard, P. C. Zhai, Q. J. Zhang, and G. J. Snyder, Chem. Mater. **27**, 6329 (2015).
[35] I. N. Frantsevich, F. F. Voronov, and S. A. Bokuta, in *Elastic Constants and Elastic Moduli of Metals and Insulators Handbook*, edited by I. N. Frantsevich (Naukova Dumka, Kiev, 1983), pp. 60–180.
[36] G. Vaitheeswaran, V. Kanchana, R. S. Kumar, A. L. Cornelius, M. F. Nicol, A. Svane, A. Delin, and B. Johansson, Phys. Rev. B **76**, 014107 (2007).
[37] B. Li, H. Sun, and C. Chen, Nat. Commun. **5**, 4965 (2014).
[38] G. D. Li, U. Aydemir, S. I. Morozov, M. Wood, Q. An, P. C. Zhai, Q. J. Zhang, W. A. Goddard, and G. J. Snyder, Phys. Rev. Lett. **119**, 085501 (2017).
[39] Y. Zheng, Q. Zhang, X. L. Su, H. Y. Xie, S. C. Shu, T. L. Chen, G. J. Tan, Y. G. Yan, X. F. Tang, C. Uher, and G. J. Snyder, Adv. Energy Mater. **5**, 1401391 (2015).
[40] P. S. Kostenetskiy and A. Y. Safonov, in *Proceedings of the 10th Annual International Scientific Conference on Parallel Computing Technologies* (Arkhangelsk, Russia, 2016).